EVM-Fusion: An Explainable Vision Mamba Architecture with Neural Algorithmic Fusion

Zichuan Yang

Abstract

Medical image classification is critical for clinical decision-making, yet demands for accuracy, interpretability, and generalizability remain challenging. This paper introduces EVM-Fusion, an Explainable Vision Mamba architecture featuring a novel Neural Algorithmic Fusion (NAF) mechanism for multi-organ medical image classification. EVM-Fusion leverages a multipath design, where DenseNet and U-Net based pathways, enhanced by Vision Mamba (Vim) modules, operate in parallel with a traditional feature pathway. These diverse features are dynamically integrated via a two-stage fusion process: cross-modal attention followed by the iterative NAF block, which learns an adaptive fusion algorithm. Intrinsic explainability is embedded through path-specific spatial attention, Vim *Delta*-value maps, traditional feature SE-attention, and cross-modal attention weights. Experiments on a diverse 9-class multi-organ medical image dataset demonstrate EVM-Fusion's strong classification performance, achieving 99.75% test accuracy and provide multi-faceted insights into its decision-making process, highlighting its potential for trustworthy AI in medical diagnostics.

Keywords: Deep Learning, Explainable AI (XAI), Vision Mamba, Neural Algorithmic Fusion, Multi-Path Architecture, Medical Image Classification

1 Introduction

The accurate and timely classification of medical images is paramount in clinical diagnostics and treatment planning, spanning diverse modalities such as X-ray, Computed Tomography (CT), and Magnetic Resonance Imaging (MRI). While human expertise remains crucial, the increasing volume and complexity

of medical imaging data presents significant challenges, including inter-observer variability and diagnostic delays [1]. Artificial Intelligence (AI), particularly deep learning, has demonstrated remarkable potential in automating and augmenting medical image analysis, promising to enhance both diagnostic efficiency and accuracy [2–4].

Early AI approaches often relied on handcrafted features capturing predefined image properties (e.g., texture, shape) [5, 6], which were then fed into traditional machine learning classifiers [7– 9]. With the widespread application of deep learning technology, especially convolutional neural networks (CNNs) [3], CNN-based approaches often focus either on direct classification using learned features [10–14] or leverage image segmentation [15] to isolate regions of interest (ROIs) before classification [16–19]. Despite their success, these models often operate as "black boxes," limiting clinical trust and adoption. Furthermore, fusing information from different architectural paradigms or feature types to achieve superior performance and generalizability remains a complex challenge. Simple concatenation or weighted averaging of features may not capture the intricate, context-dependent relationships between different feature streams.

To address these limitations, this paper proposes an Explainable Vision Mamba Architecture with Neural Algorithmic Fusion (EVM-Fusion), a novel deep learning architecture designed for robust and interpretable multi-organ medical image classification. It is a novel multi-path architecture integrating Vision Mamba (Vim) [20] for enhanced feature representation from diverse sources. What's more, it introduces of the Neural Algorithmic Fusion (NAF) block, a new iterative and adaptive fusion mechanism. Finally, the comprehensive integration of intrinsic XAI components [21] on the model provides multi-level interpretability for medical image classification. Experimental results on a challenging multi-organ medical image dataset (comprising X-rays and MRIs for 9 distinct classes) demonstrate the superior performance and robustness of EVM-Fusion, alongside providing rich insights through its explainability features. The remainder of this paper is organized as follows: Section 2 reviews related work. Section 3 details the EVM-Fusion architecture. Section 4 describes the experimental setup. Section 5 presents and discusses the results, including quantitative performance and qualitative XAI analysis. Section 6 concludes the paper.

2 Related Work

2.1 Deep Learning Architectures for Medical Image Classification

Convolutional neural networks (CNNs) have long been the dominant paradigm in medical image analysis [3]. Pioneering architectures such as AlexNet [22], VGG [23], ResNet [24], and DenseNet [25] have established powerful hierarchical feature learning capabilities. ResNet solves the vanishing gradient problem in deep networks through residual connections, while DenseNet promotes feature reuse and reduces parameters through dense connections between layers. Dual Path Networks (DPNs) [26] aim to combine the advantages of ResNet and DenseNet. U-Net [27] was originally designed for biomedical image segmentation. Due to its effective multi-scale feature extraction and local detail representation capabilities, it has also been used for classification tasks [18], and sometimes DenseNet modules are integrated in its encoder, mainly for segmentation [28-31]. Recently, Vision Transformers (ViT) [32] and its variants, such as the Swin Transformer [33], have shown promise by

applying the Transformer [34] architecture, which originally achieved success in natural language processing (NLP), to vision tasks and capturing global context through self-attention mechanisms.

2.2 Multi-Path and Multi-Modal Fusion Techniques

Integrating information from multiple sources or pathways is a common strategy to improve model performance. In medical imaging, this may involve fusing features from different network architectures (multi-path) or different imaging modalities (multi-modality). While simple concatenation or averaging, while effective, may not optimally capture complex inter-modality dependencies. More advanced fusion techniques involve attention mechanisms that dynamically weigh the contributions of different feature sets. Learning an explicit adaptive fusion algorithm represents a step towards more sophisticated integrations.

2.3 Explainable AI (XAI) in Medical Imaging

The "black box" nature of many deep learning models hinders their clinical adoption, making XAI crucial [35]. Common post-hoc XAI methods include LIME [36] and SHAP [37]. For CNNs, activation mapping techniques like CAM [38] and its derivatives (Grad-CAM, Grad-CAM++) [39] highlight image regions influencing predictions. However, building intrinsically interpretable models, where explainability is a core part of architecture, is an increasingly important research direction [40]. My EVM-Fusion incorporates multiple intrinsic XAI components at different stages.

2.4 State Space Models (SSMs) and Mamba in Vision

In recent years, state-space models (SSMs) have emerged as a powerful alternative to Transformer sequence modeling, offering linear time complexity and strong long-range dependency capture capabilities. The Mamba architecture [41] introduced a selective scanning mechanism (S6 model) to achieve inputdependent state transition modulation. This has driven the rapid development of Mamba in vision tasks. Vim and the visual state-space model (VMamba) [42] apply the advantages of Mamba to 2D image data by splicing images into sequences and adopting specialized scanning strategies (e.g., bidirectional, multidirectional). These models show comparable performance to CNNs and ViT, while being more efficient in processing long sequences.

2.5 My Contribution in Context

While existing works have explored multipath CNNs, attention-based fusion, and the application of Mamba to vision, EVM-Fusion introduces several novel contributions. Unlike standard multipath models that often use simple fusion, EVM-Fusion pioneers a Neural Algorithmic Fusion (NAF) block, which learns an iterative, adaptive fusion process guided by a controller, following an initial crossmodal attention stage. This provides a more flexible and potentially more powerful fusion paradigm than fixed attention or concatenation schemes. Furthermore, EVM-Fusion integrates Vision Mamba modules into distinct feature extraction

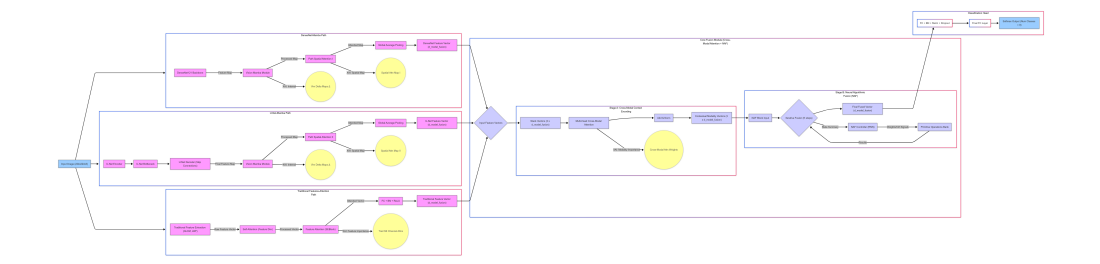


Fig. 1 The proposed EVM-Fusion architecture. The model takes a single image as input and processes it through three parallel feature extraction and enhancement paths: (1) a DenseNet-Mamba path leveraging a DenseNet121 backbone followed by a Vision Mamba module and path-specific spatial attention; (2) a U-Net-Mamba path employing a full U-Net encoder-decoder structure, with a Vision Mamba module applied to the final decoder output, followed by spatial attention; and (3) a Traditional Features-Attention path that extracts GLCM and LBP features, subsequently refined by self-attention and Squeeze-and-Excitation (SE) attention. Feature vectors from these paths are then processed by a two-stage Core Fusion Module, which first uses Cross-Modal Attention for contextual encoding of inter-path relationships, followed by a novel Neural Algorithmic Fusion (NAF) block for iterative, adaptive fusion. The final fused vector is passed to a classification head. Intrinsic Explainable AI (XAI) outputs, including spatial attention maps, Vim Δ -value maps, traditional feature importance scores, and cross-modal attention weights, are generated at various stages to provide model interpretability.

pathways (DenseNet-based and U-Netbased) to leverage their long-range modeling capabilities for different types of feature hierarchies, alongside a traditional feature path. Critically, it embeds multiple intrinsic XAI mechanisms across these paths and the fusion module, offering a more holistic and multi-faceted interpretability than typically found in complex fusion models. This combination of Mamba-enhanced diverse feature streams, a novel algorithmic fusion approach, and deep intrinsic explainability for multi-organ medical image classification distinguishes EVM-Fusion from prior art.

3 Model Architecture

The overall framework, illustrated in Fig. 1, is a multi-path network that integrates

deep learning features from diverse backbone architectures with traditional hand-crafted features, all enhanced by state-of-the-art sequence modeling and attention mechanisms. A key novelty lies in its two-stage fusion strategy, culminating in a Neural Algorithmic Fusion (NAF) block that learns an iterative process to combine information. Intrinsic explainability is a core design principle, with XAI components embedded throughout the architecture.

3.1 Overall Framework

Given an input medical image $I \in \mathbb{R}^{H \times W \times C}$ (where H, W, C are height, width, and channels respectively), EVM-Fusion employs three parallel pathways to extract a rich set of complementary features: A DenseNet-Mamba path, designed to capture global contextual information and intricate feature patterns. A U-Net-Mamba path, focused on extracting multi-scale spatial hierarchies

and detailed local information. A Traditional Features-Attention path, providing explicit, domain-relevant texture and statistical features.

Each path p in those three produces a feature vector $v_p \in \mathbb{R}^{d_{model_fusion}}$. These vectors are then fed into the Core Fusion Module, which first applies Cross-Modal Attention to model inter-path dependencies, followed by the Neural Algorithmic Fusion (NAF) block to generate a final, unified feature representation $v_{fused} \in$ $\mathbb{R}^{d_{model-fusion}}$. This v_{fused} is then passed to a classification head to predict the image class.

3.2 Feature Extraction and Enhancement Paths

Each deep learning path (DenseNet and U-Net) incorporates a Vision Mamba module for advanced sequence-based feature refinement and a path-specific spatial attention mechanism for feature recalibration and explainability.

3.2.1 DenseNet-Mamba Path

This path aims to extract robust global and hierarchical features. The input image I is first processed by a pretrained DenseNet-121 backbone (excluding its final classification layer) to obtain a rich feature map $F_D = DenseNet(I) \in$ $\mathbb{R}^{H_D \times W_D \times C_D}$. The feature map is then fed into a Vision Mamba Module. This module first uses a convolutional patch embedding layer to transform F_D into a sequence of patch tokens $X_D \in$ $\mathbb{R}^{N_p \times d_{mamba}}$, where N_p is the number of patches and d_{mamba} is the Mamba model dimension. The core of this module consists of L_M stacked Mamba (S6) blocks [41] which process the sequence bidirectionally. Each Mamba block performs:

$$x_k', z_k = W_{in}x_k + b_{in} \tag{1}$$

$$x_k'' = Conv1D(SiLU(x_k'))$$
 (2)

$$h_k = \bar{A}_k h_{k-1} + \bar{B}_k x_k''$$

$$y_k^{ssm} = C_k h_k$$
(3)
$$(4)$$

$$y_k^{ssm} = C_k h_k \tag{4}$$

$$y_k = W_{out}(SiLU(z_k) \odot y_k^{ssm} + Dx_k''$$
 (5)

for the k-th patch x_k . Where \bar{A}_k $exp(\Delta_k A)$ and $\bar{B}_k \approx exp(\Delta_k B_k)$ (Euler approximation of the continuous system h'(t) = Ah(t) + Bx(t). The parameter Δ_k acts as an input-dependent gate controlling the influence of x_k'' versus h_{k-1} , and its values are stored for XAI.

By this, the Vim module output $F'_{D,map}$ is reshaped back into a 2D feature map of dimension $\mathbb{R}^{H'_D \times W'_D \times d_{model_fusion}}$. It is then processed by a spatial attention module. Given an input feature map $F \in \mathbb{R}^{H' \times W' \times C'}$, the spatial attention generates a 2D attention map

$$M_{spat}(F'_{D,map}) = \sigma(W_{conv}([AvgPool_{ch}(F'_{D,map}); MaxPool_{ch}(F'_{D,map})]))$$
(6)

The final feature vector for this path is $v_D = GAP(F'_{D,map} \odot M_{spat}(F'_{D,map})) \in \mathbb{R}^{d_{model_fusion}}$. Where GAP() means Global Average Pooling and the map $M_{spat}(F'_{D,map})$ is saved as the Spatial Attn Map I in Fig. 1.

3.2.2 U-Net-Mamba Path

This path is designed to capture multiscale spatial information and fine-grained details critical for medical image analysis. And its processing process is similar to Section 3.2.1.

3.2.3 Traditional Features-Attention Path

This path explicitly incorporates domainrelevant handcrafted features. For a grayscale version of input I, Gray-Level Co-occurrence Matrix (GLCM) features (e.g., contrast, homogeneity, energy over multiple distances and angles) and Local Binary Pattern (LBP) histogram features are extracted, resulting in a raw feature vector $f_{raw} \in \mathbb{R}^{d_{raw}}$.

Since traditional features are not very likely to be meaningfully organized into sequences, they are not suitable for processing using the Mamba module. Instead, I applied an multi-head attention layer [34] to learn the importance of different feature dimensions.

$$f'_{trad} = MHA(f_{raw}) \in \mathbb{R}^{d_{raw}}$$
 (7)

It is then passed through an SEBlock [43]

$$s = \sigma(W_2 ReLU(W_1 f'_{trad})) \tag{8}$$

Where $W_1 \in \mathbb{R}^{(d_{raw}/r) \times d_{raw}}$ and $W_2 \in \mathbb{R}^{d_{raw} \times (d_{raw}/r)}$ are linear layers, r is the reduction ratio. The output $f''_{trad} = s \odot f'_{trad}$ and the channel-wise attention scores $s \in \mathbb{R}^{d_{raw}}$ are saved as Trad SE Channel Attns for XAI. Finally, f''_{trad} is passed through a fully connected layer with ReLU activation and Batch Normalization to produce $v_T \in \mathbb{R}^{d_{model-fusion}}$

3.3 Core Fusion Module

This module intelligently integrates the feature vectors v_D, v_U, v_T .

3.3.1 Stage A: Cross-Modal Context Encoding

The input feature vectors are stacked to form $v_{in} = [v_D; v_U; v_T] \in$

 $\mathbb{R}^{N_{paths} \times d_{model_fusion}}$, where $N_{paths} = 3$. Then V_{in} is processed by an MHA layer acting as a cross-modal attention mechanism.

$$AttendedFeatures, W_{CMA} = MHA(v_{in})$$
(9)

The attention weights $W_{CMA} \in \mathbb{R}^{N_{paths} \times N_{paths}}$ (averaged over heads) indicate the learned inter-path dependencies and are saved as Cross-Modal Attn Weights for XAI. Then a residual connection followed by Layer Normalization is applied.

$$v_{contextual} = LayerNorm(v_{in} + AttendedFeatures)$$
 (10)

3.3.2 Stage B: Neural Algorithmic Fusion (NAF) Block

The NAF block takes the contextualized vector $v_{contextual}$ and learns an iterative algorithm to fuse them.

The initial input to the NAF controller $c_0 = W_{init_ctrl}v_{contextual} + b_{init_ctrl}$, where $c_0 \in \mathbb{R}^{d_{primitive_out}}$

The controller, a Gated Recurrent Unit (GRU) [44], takes the previous fused state $S_{fused}^{(k-1)}$ and its own previous hidden state $h_{ctrl}^{(k-1)}$ to produce an output $o_{ctrl}^{(k)}$ and new hidden state $h_{ctrl}^{(k)}$

$$z_{k} = \sigma(W_{z}S_{fused}^{(k-1)} + U_{z}h_{ctrl}^{(k-1)} + b_{z} \quad (11)$$

$$r_{k} = \sigma(W_{r}S_{fused}^{(k-1)} + U_{r}h_{ctrl}^{(k-1)} + b_{r} \quad (12)$$

$$\tilde{h}_{ctrl}^{(k)} = tanh(W_{h}S_{fused}^{(k-1)} + U_{h}(r_{k} \odot h_{ctrl}^{(k-1)}) + b_{h}) \quad (13)$$

$$h_{ctrl}^{(k)} = (1 - z_{k}) \odot h_{ctrl}^{(k-1)} + z_{k} \odot \tilde{h}_{ctrl}^{(k)} \quad (14)$$

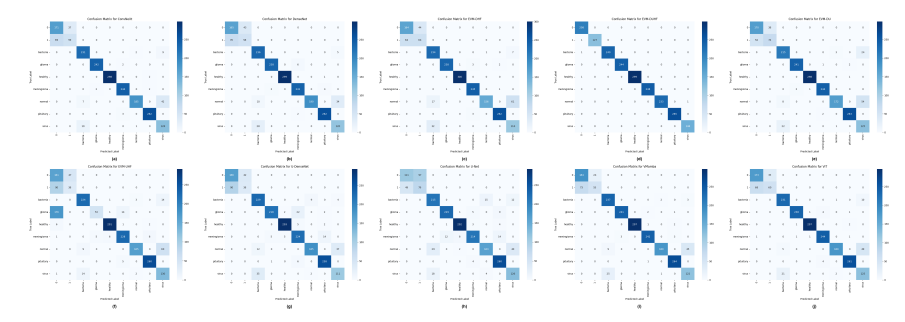


Fig. 2 The Confusion Matrices of the 10 models evaluated on the test set. To demonstrate the rationality of the model architecture, I conducted ablation experiments. In the figure, EVM-DUHF represents the complete EVM-Fusion model with the DenseNet-Mamba Path, U-Net-Mamba Path, Traditional Features-Attention Path. The other three models in the figure, EVM-DHF, EVM-DU, EVM-UHF, are variants of EVM-DUHF with the U-Net-Mamba Path, Traditional Features-Attention Path, DenseNet-Mamba Path removed, respectively. Additionally, U-DenseNet refers to the model described in [28], which uses DenseNet-121 as the encoder for U-Net.

Table 1 Dataset Summary

		Bra	in Tumor		Breast	t Cancer	Ch	Sum		
	glioma healthy meningioma p		pituitary	0	1	normal	bacteria	virus		
train	1134	1400	1151	1229	1569	803	1145	2159	1148	11638
validation	243	300	246	263	448	227	204	379	197	2507
test	244	300	248	265	208	128	234	242	148	2017
sum	1621	2000	1645	1757	2225	1158	1583	2780	1493	16162

actually $o_{ctrl}^{(k)}$ is typically $h_{ctrl}^{(k)}$ and the iterative fused state $S_{fused}^{(0)}$ is c_0 . The iteration process will be performed K_{NAF} times

The controller output $o_{ctrl}^{(k)}$ is used to generate mixing weights $\alpha^{(k)} \in \mathbb{R}^{N_{primitives}}$ for the primitive operations:

$$\alpha^{(k)} = softmax(W_{mix}o_{ctrl}^{(k)} + b_{mix})$$
 (15)

A bank of $N_{primitives}$ distinct primitive operations $\mathcal{P} = \{Prim_1, ..., Prim_{N_{primitives}}\}$ (each typically a MLP in my implementation) processes the static $v_{contextual}$:

$$P_j^{(k)} = Prim_j(v_{contextual}) \in \mathbb{R}^{d_{primitive_out}}$$
(16)

and are mixed using $\alpha^{(k)}$:

$$S_{mix}^{(k)} = \sum_{i=1}^{N_{primitives}} \alpha^{(k)} P_j^{(k)}$$
 (17)

During the iteration, I update the state using residual connection: If $k=1, S_{fused}^{(1)} = S_{mix}^{(1)}$. If $k>1, S_{fused}^{(k)} = LayerNorm(S_{fused}^{(k-1)} + S_{mix}^{(k)})$ The final output of the NAF block

The final output of the NAF block v_{NAF} , is obtained by further processing $S_{fused}^{(K_{NAF})}$ through a linear layer and Layer-norm after K_{NAF} iterations.

The NAF block's strength lies in its learned, iterative refinement. The controller (GRU) acts as a policy network, dynamically determining at each step k how to best combine the outputs of various general-purpose primitive functions (Prim_j) based on the current state of fusion $(S_{fused}^{(k-1)})$. This allows for a more adaptive and potentially deeper fusion process than a fixed set of operations. The primitives always operating on the initial comprehensive feature set

Table 2 Detailed Comparison of Model Performance Metrics with Per-Class Scores. Best values in each column are in **red**, second best in **blue**.

Model	Overall			0			1			Bacteria				Glioma			Healthy			Meningioma			Normal			Pituitary			Virus		
	Acc	P	R	F1	P	R	F1	P	R	Fi	P	R	F1	P	R	F1	P	R	Fl	P	R	Fl	P	R	Fl	P	R	Fl	P	R	F1
EVM-DUHF	0.9975	0.9975	0.9975	0.9975	0.9858	1.0000	0.9928	1.0000	0.9922	0.9961	1.0000	0.9917	0.9959	1.0000	1.0000	1.0000	1.0000	0.9967	0.9983	1.0000	1.0000	1.0000	0.9957	0.9957	0.9957	1.0000	1.0000	1.0000	0.9933	1.0000	0.9966
EVM-DHF	0.8820	0.8907	0.8820	0.8800	0.7193	0.7885	0.7523	0.5926	0.5000	0.5424	0.8269	0.9689	0.8914	0.9958	0.9754	0.9855	0.9934	1.0000	0.9967	0.9761	0.9879	0.9820	0.9936	0.6667	0.7980	0.9887	0.9887	0.9887	0.6304	0.7838	0.6388
EVM-DU	0.8934	0.9028	0.8934	0.8945	0.7556	0.8173	0.7852	0.6607	0.5781	0.6167	0.8776	0.8884	0.8830	0.9877	0.9877	0.9877	0.9967	0.9933	0.9950	0.9879	0.9839	0.9859	0.9773	0.7350	0.8390	0.9887	0.9925	0.9906	0.6158	0.8446	0.7123
EVM-UHF	0.7685	0.8291	0.7685	0.7606	0.3701	0.7740	0.5008	0.4471	0.2969	0.3568	0.9069	0.9256	0.9162	0.9138	0.2172	0.3510	0.9700	0.9700	0.9700	0.9194	0.9194	0.9194	0.9706	0.7051	0.8168	0.9630	0.9811	0.9720	0.6373	0.8784	0.7386
DenseNet[25]	0.8969	0.8986	0.8969	0.8954	0.7021	0.7933	0.7449	0.5743	0.4531	0.5066	0.8613	0.9752	0.9147	0.9835	0.9754	0.9794	1.0000	0.9967	0.9983	0.9679	0.9718	0.9698	0.9948	0.8120	0.8941	0.9813	0.9887	0.9850	0.7547	0.8108	0.7818
U-Net[27]	0.8374	0.8471	0.8374	0.8378	0.6937	0.5337	0.6033	0.4489	0.6172	0.5197	0.8206	0.8884	0.8532	0.9424	0.9385	0.9405	0.9637	0.9733	0.9685	0.9469	0.8629	0.9030	0.8956	0.6966	0.7837	0.9059	0.9811	0.9420	0.7079	0.8514	0.7730
U-DenseNet 28	0.8537	0.8526	0.8537	0.8495	0.6484	0.7981	0.7155	0.4750	0.2969	0.3654	0.8297	0.9463	0.8842	0.9732	0.8934	0.9316	0.9767	0.9767	0.9767	0.8716	0.9032	0.8871	0.9439	0.7906	0.8605	0.9348	0.9736	0.9538	0.7303	0.7500	0.7400
ViT[32]	0.8969	0.9018	0.8969	0.8958	0.7149	0.8317	0.7689	0.6316	0.4688	0.5381	0.8988	0.9545	0.9259	0.9917	0.9754	0.9835	0.9933	0.9900	0.9917	0.9683	0.9839	0.9760	0.9836	0.7692	0.8633	0.9849	0.9849	0.9849	0.6793	0.8446	0.7530
VMamba[42]	0.9033	0.9073	0.9033	0.9003	0.7160	0.8846	0.7914	0.6962	0.4297	0.5314	0.8745	0.9793	0.9240	0.9877	0.9877	0.9877	1.0000	0.9900	0.9950	0.9837	0.9758	0.9798	0.9836	0.7692	0.8633	0.9778	0.9962	0.9869	0.7176	0.8243	0.7673
ConvNeXt[45]	0.9023	0.9056	0.9023	0.9010	0.7125	0.8221	0.7634	0.6146	0.4609	0.5268	0.8988	0.9545	0.9259	0.9918	0.9918	0.9918	1.0000	0.9933	0.9967	0.9799	0.9839	0.9819	0.9840	0.7906	0.8768	0.9850	0.9887	0.9868	0.7151	0.8649	0.7829

 $(v_{contextual})$ ensures access to rich information, while the iterative state $S_{fused}^{(k)}$ allows the controller to track the fusion progress. Residual connections and LayerNorm aid in stabilizing training for multiple iterations.

4 Experiments

There are three datasets in total. One is the brain tumor MRI dataset from Kaggle [46], which contains four categories: healthy, glioma, meningioma, and pituitary. Another is the breast cancer X-ray dataset from Kaggle [47], which contains two categories: 0, 1, where 0 represents benign and 1 represents malignant. The last one is the chest X-ray dataset from Mendeley Data [48] proposed by Daniel S. Kermany et al. [49], which contains three categories: normal, bacteria, virus, where normal represents health, bacteria represents bacterial pneumonia, and virus represents viral pneumonia. The specific distribution is shown in Table 1.

All images are uniformly resized to a standard size of 224×224 pixels. A variety of data augmentation measures were taken for the images in the training set, including rotation, translation, scaling, flipping, and brightness adjustment. The models are trained on the training set and validated with early stopping on the test set. The confusion matrix is obtained on the test set, as shown in Fig. 2. Based on the confusion matrix, other evaluation indicators are calculated, as shown in Table 2.

5 Discussion

The EVM-Fusion model demonstrates strong classification performance, underscoring its potential for robust multiorgan medical image analysis. Beyond quantitative metrics, a central aim was achieving intrinsic interpretability. This section discusses insights from the model's built-in eXplainable AI (XAI) mechanisms, analyzing its behavior on correctly classified (Fig. 4) and misclassified (Fig. 3) samples to elucidate its operational dynamics and the benefits of its architecture.

Vision Mamba's Adaptive Processing (Δ -value Maps): The Δ -value maps from the Vision Mamba modules reveal dynamic, input-dependent information gating. Higher Δ values (warmer colors) signify a greater emphasis on current patch information, indicating regions of novelty or high salience. Conversely, lower Δ values (cooler colors) suggest reliance on previously propagated contextual states, often where information is redundant or predictable. For instance, in a correctly classified "normal" chest Xray (Fig. 4g), the DenseNet path's Vim Δ maps show adaptive focus: the forward scan emphasizes lung boundaries upon encountering them, while the backward scan might highlight different boundary segments. The U-Net path's Vim modules on the same sample might show more detailed, localized Δ peaks within the lung fields. Comparing forward and backward Δ maps (e.g., Fig. 4b, a malignant tumor) often reveals differing "novelty"

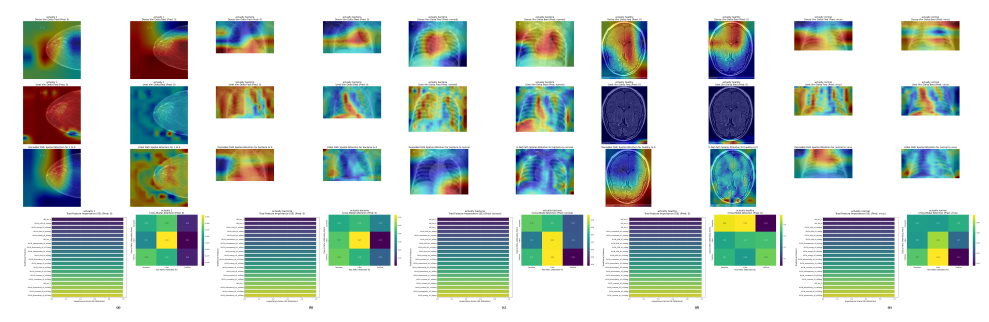


Fig. 3 Explainable AI (XAI) Analysis of Representative Misclassified Test Samples by EVM-DUHF. This figure presents a consolidated view of intrinsic explainability outputs for five misclassified samples from the 9-class test set. Noted from (a) to (e). Each sample is analyzed using eight distinct XAI visualizations. From top to bottom, from left to right, they are DenseNet Vision Mamba Forward Δ Map, DenseNet Vision Mamba Backward Δ Map, U-Net Vision Mamba Forward Δ Map, U-Net Vision Mamba Backward Δ Map, DenseNet Path Spatial Attention, U-Net Path Spatial Attention, Traditional Feature Importance (SE Attention bar plot), Cross-Modal Attention Weights (heatmap). These visualizations aim to elucidate the model's internal feature prioritization and fusion dynamics in instances of incorrect classification, providing insights into potential failure modes and areas of confusion.

assessments based on the directional context of Mamba's selective scan, showcasing its capacity for nuanced contextual understanding.

Path-Specific Spatial Attention: The spatial attention maps for the DenseNet and U-Net Mamba paths highlight prioritized image regions before global feature aggregation. In a correctly identified malignant tumor (Fig. 4b), these maps focus on the breast tissue, with DenseNet potentially emphasizing broader areas while U-Net targets more specific regions like the nipple, possibly indicating sensitivity to microcalcifications or lesion-dense areas. Interestingly, Fig. 4b also reveals a potential U-Net flaw, with some attention on blank image edges, underscoring the value of multipath fusion to mitigate individual path imperfections.

Traditional Feature Importance (SE-Attention): The Squeeze-and-Excitation (SE) attention weights within the traditional feature path quantify the contribution of specific GLCM and LBP

features. For a correctly classified "normal" lung (Fig. 4g), features indicative of textural uniformity (LBP_bin_5 and LBP_bin_6) are often highly weighted. This demonstrates the model's ability to leverage well-understood handcrafted features that complement deep learned representations, capturing intrinsic textural properties relevant to the diagnostic class.

Cross-Modal Attention: A cornerstone of EVM-Fusion's adaptability is the dynamic nature of its cross-modal attention weights, which vary significantly across different input images (Fig. 4). For the benign tumors (Fig. 4a), all paths show increased attention towards the U-Net path, suggesting a reliance on its detailed local information for tumor characterization. Conversely, for a "healthy" brain MRI (Fig. 4e), the attention shift, with U-Net drawing more from the traditional path if specific textures are key. This input-dependent, flexible weighting

allows EVM-Fusion to adaptively modulate the influence of each feature pathway prior to the final Neural Algorithmic Fusion (NAF) stage. Notably, across many samples in Fig. 4, most paths often receive substantial attention (e.g., ¿25-30%), indicating their collective importance and complementary roles. This inherent dynamism and balanced contribution underpin the superior performance of the full 3-path EVM-Fusion (EVM-DUHF) over ablated versions lacking one or more paths, as it allows the model to maximize information gain from diverse feature types and reduce overreliance on any single potentially fallible source.

For (a) in Fig.3, both DenseNet and U-Net only focus on the same area of the breast. The model judges the malignant tumor (1) as benign (0), which indicates that there may be no tumor in this area. For (b) and (d) in Fig.3, it can be found that the DenseNet path focuses on the lower right corner, and U-Net pays almost no attention to the human body. This causes the model to even make crosscategory errors, mistaking photos of the brain and chest for breasts. And (c) and (e) in Fig.3 also make the same mistake. Neither DenseNet nor U-Net pays good attention to the key organ - the lungs.

Through the above analysis, the clinical application of the model can be enhanced. By analyzing these heat maps, if the model's paths do not pay enough attention to the potential lesion area, even doctors who know nothing about the model principle can know that the output is unreliable. On the contrary, if both models pay attention to the organs that need attention, especially the U-Net path, then even if the doctor does not believe the output of the model, he can focus on the places that U-Net pays attention

to and overlaps with the organs, because those places are likely to be the location of the lesions.

6 Conclusion

In this paper, I have introduced EVM-Fusion, a novel deep learning architecture designed to address the intricate demands of multi-organ medical image classification by synergizing advanced feature extraction, dynamic fusion, and intrinsic explainability. My approach leverages a multipath framework where Vision Mamba modules enhance features from DenseNet and U-Net backbones, complemented by a dedicated path for traditional handcrafted features. The core innovation lies in our two-stage fusion strategy, particularly the Neural Algorithmic Fusion (NAF) block, which, preceded by cross-modal attention, learns an iterative, adaptive algorithm to optimally combine diverse feature streams. This NAF mechanism, incorporating a controller that observes previous fusion states and utilizes residual connections, represents a significant departure from static fusion techniques.

Experimental validation on a challenging 9-class dataset, encompassing Xrays and MRIs from multiple organ systems, demonstrated the efficacy of EVM-Fusion, achieving excellent classification accuracy of 99.75% on the test set. The detailed XAI analysis, presented in Section 5 (Discussion), further elucidated the model's behavior, showcasing its ability to dynamically focus on salient image regions, adaptively weigh features from different paths based on input characteristics (as evidenced by varying crossmodal attention), and leverage specific textural and structural cues identified by both deep and traditional feature sets.

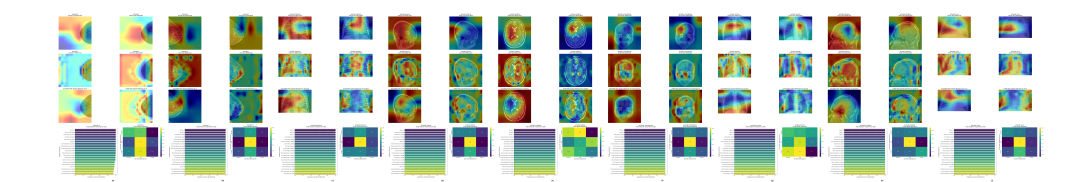


Fig. 4 Explainable AI (XAI) Analysis of Representative Correctly Classified Test Samples by EVM-DUHF Across All Classes. This figure showcases the intrinsic explainability outputs for nine correctly classified samples, one from each of the distinct medical image classes in the test set. Noted from (a) to (i). Similar to Fig. 3, each sample is depicted through eight XAI visualizations. The analysis of these diverse, correctly classified instances aims to demonstrate the model's adaptive behavior, the varying contributions of its different pathways, and its ability to focus on salient, class-relevant features across multiple organ types and imaging modalities.

This dynamic interplay, particularly the adaptive path weighting via cross-modal attention feeding into the NAF block, likely contributes to the model's robustness and superior performance compared to architectures relying on simpler or static fusion.

In conclusion, EVM-Fusion offers a powerful, interpretable, and generalizable framework for medical image classification. By combining cutting-edge representation learning with a novel algorithmic fusion strategy and a strong emphasis on explainability, this work paves the way for more trustworthy and effective AI-driven solutions in medical diagnostics.

References

- Li, F. et al. Inter-Observer and Intra-Observer Variability in Gross Tumor Volume Delineation of Primary Esophageal Carcinomas Based on Different Combinations of Diagnostic Multimodal Images. Front. Oncol. 12, 817413 (2022). PMID: 35433413; PMCID: PMC9010659.
- [2] Demir, B. & Ertürk, S. Improving SVM classification accuracy using a hierarchical approach for hyperspectral images, 2849–2852 (2009).

- [3] Li, Z., Liu, F., Yang, W., Peng, S. & Zhou, J. A Survey of Convolutional Neural Networks: Analysis, Applications, and Prospects. *IEEE Transac*tions on Neural Networks and Learning Systems 33, 6999-7019 (2022).
- [4] Nazir, M., Wahid, F. & Khan, S. A. A simple and intelligent approach for brain MRI classification. Journal of Intelligent & Fuzzy Systems 28, 1127–1135 (2015). URL: https://journals.sagepub.com/doi/ abs/10.3233/IFS-141396.
- [5] Li, B., Li, W. & Zhao, D. Multi-scale feature based medical image classification, 1182–1186 (2013).
- [6] Li, Q. et al. Medical image classification with convolutional neural network, 844–848 (2014).
- [7] Bertalya, Prihandoko, Kerami, D. & Kusuma, T. M. Classification of X-Ray Images Using Grid Approach, 314–319 (2008).
- [8] Rissati, J. V., Molina, P. C. & Anjos, C. S. Hyperspectral Image Classification Using Random Forest and Deep Learning Algorithms, 132–132 (2020).

- [9] Rui, S. Medical CT Images Classification Model Based on BBO-HS Algorithm Optimized SVM, 1053– 1057 (2020).
- [10] Jiang, Y., Chen, L., Zhang, H. & Xiao, X. Breast cancer histopathological image classification using convolutional neural networks with small SE-ResNet module. *PLoS ONE* 14, e0214587 (2019).
- [11] Korolev, S., Safiullin, A., Belyaev, M. & Dodonova, Y. Residual and plain convolutional neural networks for 3D brain MRI classification, 835–838 (2017).
- [12] Roth, H. R. et al. Anatomy-specific classification of medical images using deep convolutional nets, 101–104 (2015).
- [13] Lu, Y. Image Classification Algorithm Based on Improved AlexNet in Cloud Computing Environment, 250–253 (2020).
- [14] Zheng, Z. et al. The Combine of GLCM and Group, Focuses on the Grayscale of Medical Images, Vol. 2024, 1–4 (2024). PMID: 40038986.
- [15] Shi, J. & Malik, J. Normalized cuts and image segmentation. *IEEE Transactions on Pattern Analysis and Machine Intelligence* **22**, 888–905 (2000).
- [16] Li, Z. et al. LViT: Language Meets Vision Transformer in Medical Image Segmentation. IEEE Transactions on Medical Imaging 43, 96– 107 (2024).

- [17] Ling, Y. et al. MTANet: Multi-Task Attention Network for Automatic Medical Image Segmentation and Classification. IEEE Transactions on Medical Imaging 43, 674– 685 (2024).
- [18] Shovon, I. I., Ahmad, I. & Shin, S. Segmentation Aided Multiclass Tumor Classification in Ultrasound Images using Graph Neural Network, 1012–1015 (2025).
- [19] Shovon, I. I., Ahmad, I. & Shin, S. Segmentation Aided Multiclass Tumor Classification in Ultrasound Images using Graph Neural Network, 1012–1015 (2025).
- [20] Zhu, L. et al. Vision Mamba: Efficient Visual Representation Learning with Bidirectional State Space Model, 1–14 (JMLR.org, Vienna, Austria, 2024).
- [21] Muoka, G. W. et al. A novel attention-based explainable deep learning framework towards medical image classification, 1–8 (2023).
- [22] Krizhevsky, A., Sutskever, I. & Hinton, G. E. Imagenet classification with deep convolutional neural networks. *Commun. ACM* 60, 84–90 (2017). URL https://doi.org/10.1145/3065386.
- [23] Simonyan, K. & Zisserman, A. Very deep convolutional networks for large-scale image recognition (2014). arXiv:1409.1556.
- [24] He, K., Zhang, X., Ren, S. & Sun, J. Deep Residual Learning for Image Recognition, 770–778 (2016).

- [25] Huang, G., Liu, Z., Van Der Maaten, L. & Weinberger, K. Q. Densely Connected Convolutional Networks, 2261–2269 (IEEE Computer Society, Los Alamitos, CA, USA, 2017). ISSN: 1063-6919. URL: https://doi.ieeecomputersociety. org/10.1109/CVPR.2017.243.
- [26] Chen, Y. et al. Dual path networks, NIPS'17, 4470–4478 (Curran Associates Inc., Red Hook, NY, USA, 2017).
- [27] Ronneberger, O., Fischer, P. & Brox, T. Navab, N., Hornegger, J., Wells, W. M. & Frangi, A. F. (eds) U-Net: Convolutional Networks for Biomedical Image Segmentation. (eds Navab, N., Hornegger, J., Wells, W. M. & Frangi, A. F.) Medical Image Computing and Computer-Assisted Intervention MICCAI 2015, 234–241 (Springer International Publishing, Cham, 2015). ISBN: 978-3-319-24574-4.
- [28] Sarparrah, A. G. et al. U-DENSENET Deep Learning Model for Medical Image Segmentation. VAWKUM Transactions on Computer Sciences 12, 112–122 (2024). https://vfast.org/journals/index.php/VTCS/article/view/1922.
- [29] Thirusangu, N. & Almekkawy, M. Segmentation of Breast Ultrasound Images using Densely Connected Deep Convolutional Neural Network and Attention Gates, 1–4 (2021).
- [30] Thirusangu, N. Segmentation of Lesions from Breast Ultrasound Images using Deep Convolutional

- Neural Network (2021). Electronic Thesis/Dissertation, Pennsylvania State University. Available: https://etda.libraries.psu.edu/catalog/26490nxt359.
- [31] Gaj, S. et al. Deep learning-based automatic pipeline for quantitative assessment of thigh muscle morphology and fatty infiltration. Magn. Reson. Med. 89, 2441–2455 (2023). Epub 2023 Feb 6. PMID: 36744695; PMCID: PMC10050107.
- [32] Dosovitskiy, A. et al. An Image is Worth 16x16 Words: Transformers for Image Recognition at Scale (2021). https://openreview.net/forum?id=YicbFdNTTy.
- [33] Liu, Z. et al. Swin Transformer: Hierarchical Vision Transformer Using Shifted Windows, 10012–10022 (2021).
- [34] Vaswani, A. et al. Attention is all you need, NIPS'17, 6000–6010 (Curran Associates Inc., Red Hook, NY, USA, 2017).
- [35] Reddy, S. Explainability and Artificial Intelligence in Medicine. *The Lancet Digital Health* 4, e214–e215 (2022).
- [36] Ribeiro, M. T., Singh, S. & Guestrin, C. Why Should I Trust You?": Explaining the Predictions of Any Classifier, 1135–1144 (Association for Computing Machinery, New York, NY, USA, 2016). ISBN: 9781450342322. URL: https://doi.org/10.1145/2939672.2939778.
- [37] Lundberg, S. M. & Lee, S.-I. A unified approach to interpreting

- model predictions, 4768–4777 (Curran Associates Inc., Red Hook, NY, USA, 2017). ISBN: 9781510860964.
- [38] Zhou, B., Khosla, A., Lapedriza, A., Oliva, A. & Torralba, A. Learning Deep Features for Discriminative Localization, 2921–2929 (IEEE Computer Society, Los Alamitos, CA, USA, 2016). ISSN: 1063-6919. URL: https://doi.ieeecomputersociety.org/10.1109/CVPR.2016.319.
- [39] Selvaraju, R. R. et al. Grad-CAM: Visual Explanations from Deep Networks via Gradient-Based Localization, 618–626 (2017).
- [40] Arjunan, G. Implementing Explainable AI in Healthcare: Techniques for Interpretable Machine Learning Models in Clinical Decision-Making. International Journal of Scientific Research and Management (IJSRM) 9, 597–603 (2021).
- [41] Gu, A. & Dao, T. Mamba: Linear-Time Sequence Modeling with Selective State Spaces (2023). arXiv:2312.00752.
- [43] Hu, J., Shen, L. & Sun, G. Squeezeand-Excitation Networks, 7132–7141 (2018).
- [44] Cho, K. et al. Moschitti, A., Pang,B. & Daelemans, W. (eds) Learning Phrase Representations using

- RNN Encoder–Decoder for Statistical Machine Translation. (eds Moschitti, A., Pang, B. & Daelemans, W.) Proceedings of the 2014 Conference on Empirical Methods in Natural Language Processing (EMNLP), 1724–1734 (Association for Computational Linguistics, Doha, Qatar, 2014). https://aclanthology.org/D14-1179/.
- [45] Liu, Z. et al. A ConvNet for the 2020s, 11966-11976 (2022).
- [46] rm1000. Brain Tumor (MRI Scans). Kaggle. Available at https://www.kaggle.com/datasets/rm1000/brain-tumor-mri-scans. Accessed: Oct. 26, 2024.
- [47] HAYDER. Breast Cancer. Kaggle. Available at https://www.kaggle.com/datasets/hayder17/breast-cancer-detection. Accessed: Oct. 26, 2024.
- [48] Kermany, D., Zhang, K. & Goldbaum, M. Labeled Optical Coherence Tomography (OCT) and Chest X-Ray Images for Classification (2018). Mendeley Data, V2, https://doi.org/10.17632/rscbjbr9sj.2.
- [49] Kermany, D. S. et al. Iden-Medical Diagnoses tifying and Treatable Diseases by Image-Based Deep Learning. Cell172. 1122-1131.e9 (2018).ISSN: 0092-8674. URL: https: //www.sciencedirect.com/science/ article/pii/S0092867418301545.